Simultaneous measurement of film thickness and wave velocity in liquid-film flow with an optical fiber probe, micro-fabricated by a femtosecond pulse laser

Full Length Paper

Simultaneous measurement of film thickness and wave velocity in liquid-film flow

with an optical fiber probe

micro-fabricated by a femtosecond pulse laser

Hajime Furuichi[1] and Yuki Mizushima[2,*]

[1]Environment and Energy Systems, Graduate School of Science and Technology, Shizuoka University, Shizuoka, Japan

[2] Department of Mechanical Engineering, Graduate School of Integrated Science and Technology, Shizuoka University, Shizuoka, Japan

Corresponding author: Dr. Yuki Mizushima, Department of Mechanical Engineering, Graduate School of Integrated Science and Technology, Shizuoka University 3-5-1 Johoku, Naka-ku, Hamamatsu, Shizuoka, 432-8561, Japan. Email: mizushima.yuhki@shizuoka.ac.jp

ABSTRACT

Measuring the wavy motion of the liquid-film interface is necessary for controlling the transportation efficiency of heat and mass transfer. Such a locally and temporally minor perturbation interacts with the flow rate, liquid-film thickness, surface wave velocity, interfacial-/wall-shear stresses, and more. To reveal those interaction, we conducted the present study to develop a new intrusive optical technique for an optical fiber probe micro-fabricated by a femtosecond pulse laser (Fs-TOP) for the direct and simultaneous measurements of the liquid-film thickness and wave velocity. The Fs-TOP is a two-in-one sensor with a single fiber. Its tapered and wedge-shaped 10-μm-dia. tip is one sensor, and another is micro-fabricated in the tip's immediate vicinity. Both sensors detect the surrounding phase, and therefore the time difference of the local phase detection with the sensors is used to accurately calculate the wave velocity with superior spatial resolution. Herein, we fixed the Fs-TOP horizontally to the channel bottom and set the sensing tip point against the gas flow. The results confirmed a basic measurement principle for the time-average thickness of the liquid film and wave velocity, respectively, in verification experiments. In the verification experiment for the thickness measurement, we vertically traversed an installed height of the Fs-TOP and calculated the liquid-film ratio from the output signal at every height. We observed that the installed height equaled the time-average thickness of 0.46 [mm] when the liquid-film ratio as 56%. An analysis using random waves indicated that the de-wetting process of the Fs-TOP caused 3% error of the average thickness. In the wave-velocity measurement experiment, we compared the results obtained with the Fs-TOP with those of a laser-induced fluorescence visualization. The results demonstrated that the Fs-TOP data were in good agreement with those of the visualization within 15% accuracy. We also evaluated the uncertainties in the wave-velocity measurement by performing a 3D ray-tracing simulation of the Fs-TOP.

1. Introduction

Gas-liquid interfacial flows, so-called 'liquid-film flows,' are widely encountered in many industrial apparatuses; e.g., chemical reactors and electrical power plants. Manufacturers hope to control the heat and mass transfer at complex boundaries which are usually characterized by the flow rate, liquid-film thickness, surface wave velocity, interfacial-/wall-shear stresses, and more [1–5]. Indeed, locally and temporally minor perturbations of those parameters have the potential to significantly influence transport efficiency, e.g., regarding disturbance waves involving the notorious dry-out on nuclear fuel rods [6–9]. The measurement of the wavy liquid films at high resolution is therefore necessary to ensure the safe and efficient operation of the apparatuses.

Several research groups have reported novel techniques for estimating liquid-film thicknesses based on electricity, ultrasound, and X-rays [10–16]. These thickness resolutions are satisfactory for detecting the thickness of μm-order films, but their temporal and spatial resolutions are limited to up to 10 [kHz] and a few millimeters respectively at best. A non-intrusive optical technique has been developed over the past decades [17–19]. Its temporal resolution can exceed MHz-frequency, which is superior to the other principles if it were not for any interruptions [20]. Ohba designed an optical-fiber-based film sensor [21,22]. In the method using this sensor, two or more optical fibers that are fixed vertically to the channel bottom measure the liquid film passing above the fibers, that is, some of the fiber are used for irradiating input laser beams, and others are used for receiving reflected laser beams. The film thicknesses are calculated by measuring the intensity of the received beams and the wave velocities by the cross-correlation between the signals of the fibers. Importantly, remarkable advantages of the fiber-optic techniques are the arbitrary points-wise-measurement and noise-robustness as confirmed in recent fiber-optic communication. However, even though μm-order films are successfully detected non-intrusively, it remains difficult to measure wavy films because non-intrusive measurements cannot distinguish interfaces' shapes, local curvature, or angle. The fiber-optic techniques [17-22] is thus applicable to quiet flow, but it is difficult

to detect the disturbance waves which provide informative evidence of eddy motion, entrainment into the gas core, and shear stress at the interface [5, 23–27]. This is an inevitable drawback of the non-intrusive optical method, and a solution for it has not been identified. Therefore, the most important challenge for detecting transient motions of a liquid-film flow is neither the thickness resolution nor the temporal resolution; rather, it is the spatial resolution.

In the present study, we focused on the spatial resolution and developed a new intrusive optical technique that uses an optical fiber probe micro-fabricated by a femtosecond pulse laser (Fs-TOP) for direct and simultaneous measurements of liquid-film thicknesses and wave velocities. The optical fiber probes are applied in a local phase detection method for dispersed gas-liquid two-phase flows [28–35]. The Fs-TOP is a two-in-one sensor with a single fiber, which allows us to measure velocities. Common sense would suggest that two fibers are needed to measure the velocity, but this would restrict the spatial resolution due to the fiber diameter. In our Fs-TOP, the distance between the sensors is dozens of μm at minimum, and the common sampling rate of the photoelectric conversion device is over MHz; the measurement of the interfacial velocity at the order of m/s at very local region is thus achieved, in principle. Liquid-film measurements are easily affected by the interfaces' shapes, as mentioned above. In these contexts, the Fs-TOP has the potential to enable liquid-film measurements with the best spatial and time resolutions.

Herein, we tested the performance of the new Fs-TOP for liquid-film measurements. The sensing tip of the Fs-TOP has a 10-μm diameter and a tapered wedge-shape. It is fixed horizontally to the channel bottom for the measurements. We first tested a basic measurement principle for time-average thicknesses of liquid films and wave velocities in experiments. Then, based on a calibration test using visualization with a high-speed camera, we experimentally tested the method for measuring film thicknesses. Finally, for the investigations of the Fs-TOP's measurement of wave velocities, we compared the results obtained using the Fs-TOP with those from the laser-induced

fluorescence (LIF) visualization. The results demonstrated that the wave velocity measured by the Fs-TOP was in good agreement with the LIF visualization, within 15% accuracy.

2. Basics of liquid-film measurement with the single-tip optical fiber probe microfabricated by femtosecond pulse laser (Fs-TOP)

2.1. Optical setup

The Fs-TOP is a multimode step-index fiber (core dia. 100 [μm], clad thickness 20 [μm]) made of quartz, as shown in Figure 1. The fiber end was processed to a taper with the use of a micropipette puller (P-2000, Sutter Instruments, Novato, CA). The tapered tip of the Fs-TOP was precisely processed to a 10-μm dia. with a 32° wedge angle by diamond polishing. We processed the water-repellent finish on the tapered surface of the Fs-TOP to avoid droplet adhesion. The tip diameter was determined based on the minimum size that could function as a sensor, and the wedge angle was determined based on the optimization to detect the gas-liquid interface with a higher signal-to-noise ratio [33]. Here, what we call the sensor is the part that detects the 'phase change' (i.e., gas-liquid interface). The optical fiber consists of a core and a cladding layer, and the exposed fiber-core works as the sensor. The small 50-μm-wide groove that was microfabricated around the outside of the tip by a femtosecond pulse laser [28] functions as a second sensor. The Fs-TOP thus has two sensors at the same fiber, and it can therefore measure the interfacial velocity with high spatial resolution (see also Appendix A).

Figure 2 provides an outline of the probing system. A laser diode (wavelength 635 [nm], output 3 [mW]) is used as the light source. The laser beams passing through a beam splitter are focused on the inlet tip of the Fs-TOP by an objective lens. The incident laser beams reach the sensors of the Fs-TOP. The laser beams that reach the sensors are reflected or refracted, and then some of the laser beams return into the inlet tip; they are extracted by the beam splitter and a polarizer. Finally, the returned laser beams are converted to electrical signals by a photomultiplier. A digital oscilloscope records the

electrical signals as output. The intensity of the returned beams depends on the difference in refractive indices between the optical fiber (1.44) and the fluid surrounding the sensors, the air (1.00), and/or water (1.33).

Figure 3 is a schematic of the relationship between the surrounding phase of the sensors and the returned beam intensity. We observed that when the top sensor S1 and the groove sensor S2 were positioned in the air, the returned beam intensity was high (Fig. 3-i). When only the top sensor S1 was positioned in water, the returned beam intensity became lower (Fig. 3-ii). After both sensors S1 and S2 were covered with the water, the returned beam intensity further decreased (Fig. 3-iii). Consequently, the interfaces passing through the sensors of the Fs-TOP could be detected from the output signal of the returned laser beams .
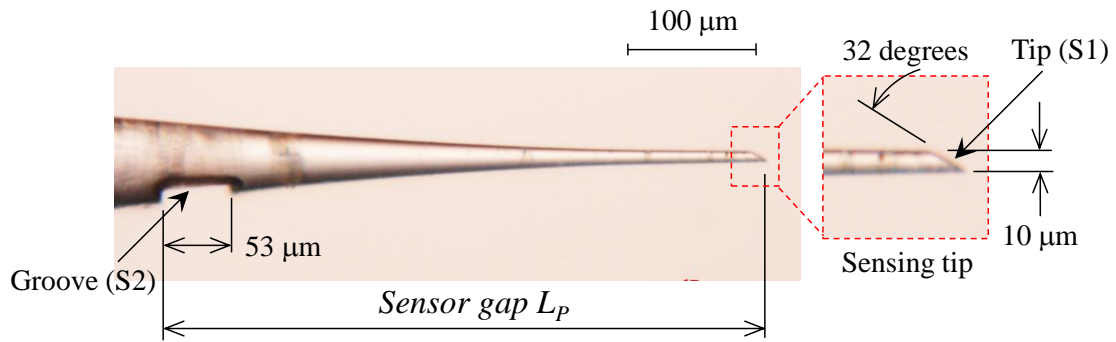
Fig. 1. A micrograph of the Fs-TOP.
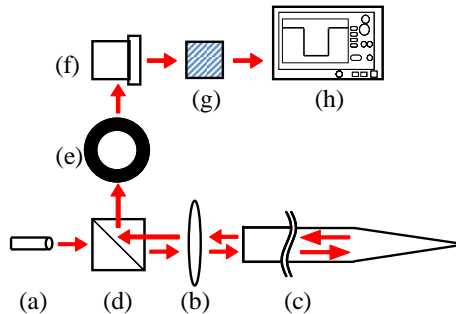
Fig. 2. An outline of the probing system of the Fs-TOP. **(a)** Laser diode, **(b)** objective lens, **(c)** Fs-TOP, **(d)** beam splitter, **(e)** polarizer, **(f)** photomultiplier, **(g)** amplifier,

and **(h)** digital oscilloscope.
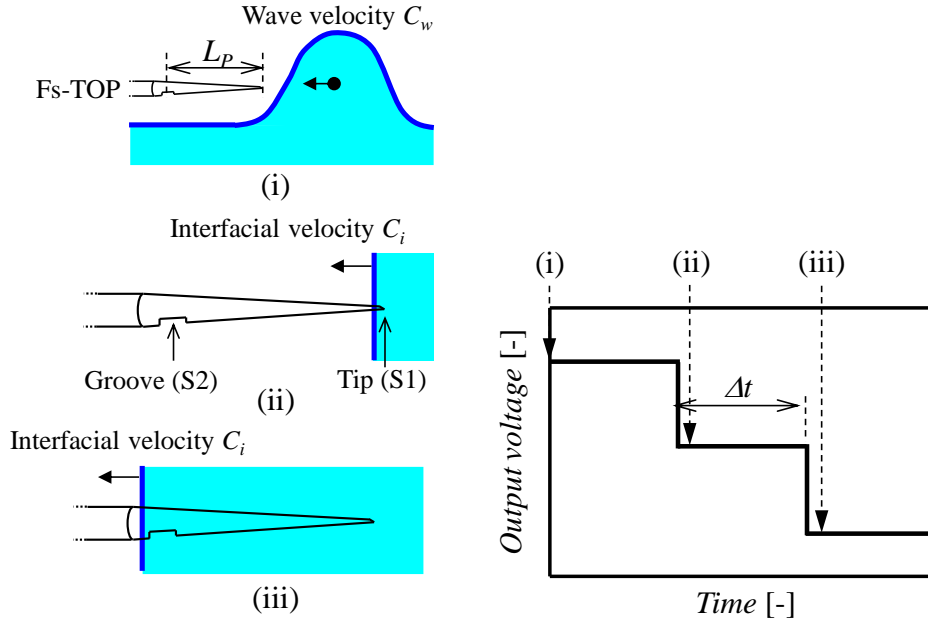
Fig. 3. Returned beam intensity from the Fs-TOP.

2.2. Measurement method for liquid-film thicknesses and wave velocities

A typical output signal from the Fs-TOP is shown in Figure 4. Here, the signal was down-sampled for thickness measurement, and thus the step-like signals are not shown. The Fs-TOP was installed in parallel to the channel base, and the sensing tip was directed against the flow. The high-speed images (i) and (ii) are visualized at the time points (i) and (ii) in the output signal, respectively. As mentioned above, the intensity of the returned beams in the Fs-TOP depends on the refractive indices surrounding the sensing tip. The output voltage thus rises to a high value, defined as the gas level V_G when the sensing tip is positioned in an air flow at the time (i). Inversely, when the sensing tip is positioned in a liquid film flow, the output voltage is a low value defined as the liquid level V_L at the time (ii). To determine the surrounding phase through the signal processing, we use a lower threshold, V_{th1}.
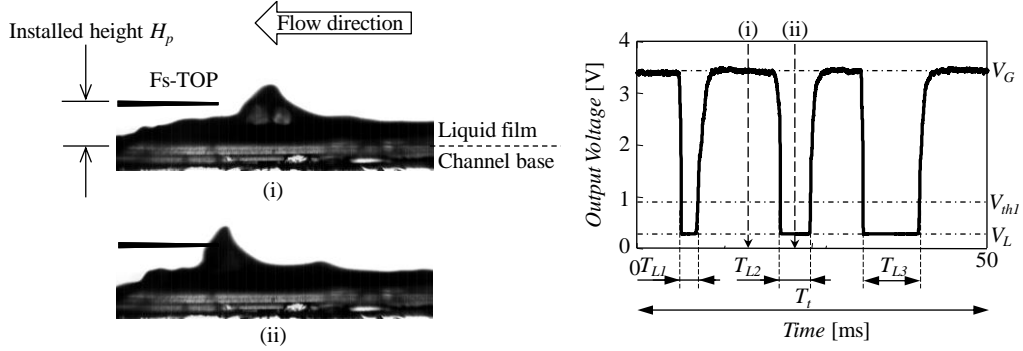
Fig. 4. Typical output signal of the Fs-TOP.

2.2.1. Liquid-film thickness measurement

For the measurement of the liquid-film thickness, the liquid-film ratio (β) is calculated from the output signal of the Fs-TOP with the following equation:

$$\beta = \frac{\sum T_L}{T_t} = \frac{T_{L1} + T_{L2} + ... + T_{L(n-1)} + T_{Ln}}{T_t} \tag{1}$$

Here, T_L is the measurement time in which the sensing tip is in the liquid film [s]; T_t is the total measurement time, and n is detection number of T_L during T_t. The relationship between the output signal and Eq. (1) is demonstrated in Figure 4 with n=3. According to Eq. (1), $(1-\beta)$ is equal to the local void fraction.

The measurement procedure is as follows: (i) the calculation of β at the channel base, using an arbitrary duration; (ii) the traversal of the installation height of the Fs-TOP vertical to the channel base, and then the calculation of β using the same duration; and (iii) the identification of the position at which the Fs-TOP is completely exposed in the gas phase (β=0). During this procedure, one can see that the liquid-film ratio β decreases with the Fs-TOP traversed. The average film thickness is defined at the position of β=0.5 [29].

The threshold has been determined via the histogram method [31]: (i) the calculation of a histogram of the output voltage as shown in Figure 5; (ii) the selection of

two of the highest peaks as the gas level V_G and the liquid level V_L, respectively; (iii) defining the 20% level of the difference between V_G and V_L as the lower threshold V_{th1}; and (iv) the calculation of T_L according to the following equations:

$$T_L = \frac{1}{f_s} \sum_{t=0}^{T_t} n_t \tag{2}$$

$$n_t = \begin{cases} 1 & (V < V_{th1}) \\ 0 & otherwise \end{cases} \tag{3}$$

Here, f_s is the sampling rate [Hz], V is the output voltage [V], and n_t is the number of discrete data in the output signal [−]. The liquid film is defined when the output voltage of $V < V_{th1}$, and then n_t is counted in Eq. (3). It must be noted that the purpose of the histogram method is to avoid the spike noise effect [33]. The output signal sometimes includes some spike noises (as shown in Fig. 6i–iii) due to incomplete phase detection. When the liquid-film thickness is almost the same as the installation height of the Fs-TOP, the sensors are partially and temporarily exposed to either phase or both phases because the sensors have very small but finite areas. This results in unstable signal level shapes with a positive/negative spike. To avoid such spike noises, a higher threshold V_{th2} is additionally introduced.
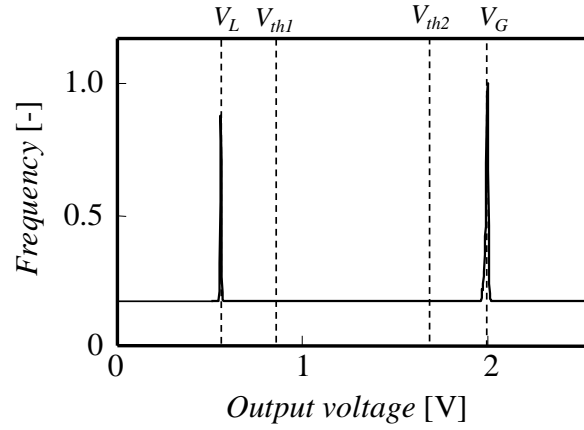
Fig. 5. Histogram of the output signal form the Fs-TOP.
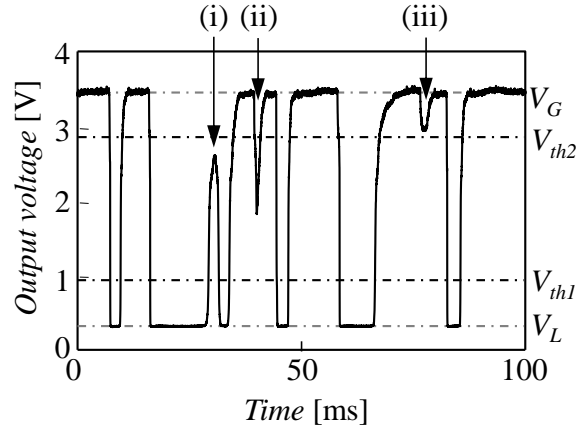
Fig. 6. Example of spike noises.

The phase change from the liquid film to the air is detected only when the output voltage exceeds the higher threshold V_{th2}. In this situation, the positive spike noise (Fig. 6-i) avoids being counted as the air phase, instead, the surrounding phase is determined as liquid film. The phase change from the air to the liquid film is detected only when the output voltage becomes less than the lower threshold V_{th1}. In this situation, the negative spike noises (Fig. 6-ii,iii) avoid being counted as the liquid phase; instead, the surrounding phase is determined as the air. The thresholds V_{th1} and V_{th2} are calculated by the following equations:

$$V_{th1} = V_L + \gamma\left(V_G - V_L\right) \tag{4}$$

$$V_{th2} = V_G - \gamma\left(V_G - V_L\right) \tag{5}$$

Here, V_{th1} is a lower threshold [V] and V_{th2} is a higher threshold [V]. The variable γ is the determination rate [−], and $\gamma = 20\%$ has been determined. We have thus achieved a precise and fast signal-processing method for thickness measurement.

2.2.2. Wave-velocity measurement

In a liquid-film flow with high air velocity, the liquid-film surface is disturbed and fluctuates due to the increase in the interfacial shear stress. In particular, a disturbance wave slides on the thin base film [15]. The wave velocity is defined as the sliding velocity of the wavy surface in the flow direction. Other research groups have calculated the wave velocity from the cross-correlation between the measured results of time-series local-thicknesses at two distant points [36, 37]. This method is applicable only under the assumption that the entire surface shape of the disturbance wave does not change immediately. The Fs-TOP can clearly detect waves without such an assumption. Figure 3 illustrates the theoretical relationships in wave-velocity measurements by the Fs-TOP. The local interfacial velocity C_i [m/s] is calculated by the following equation:

$$C_i = \frac{L_P}{\Delta t} \tag{6}$$

Here, L_P is the sensor gap between the sensing tip and the groove (440 [μm], Fig. 1), and Δt is the time lag of the phase detection. The time lag Δt is calculated an output signal from the Fs-TOP. Figure 3-ii is the time point at which the gas-liquid interface contacts the top sensor, and Figure 3-iii is the time point at which the gas-liquid interface contacts the groove sensor. The time lag Δt is thus theoretically determined as the time difference

between time points (ii) and (iii).

3. Experimental setup and conditions for liquid-film measurement

To test our novel technique, we measured a co-current gas/liquid flow in a horizontal channel. A schematic of the experimental setup is provided in Figure 7. Compressed air from the compressor was introduced into a test section which was an acrylic rectangle channel. The channel was 20 [mm] wide and 30 [mm] high. The water was injected from a vessel to the channel bottom by a pump, and the liquid-film flow was generated in the test section. The flow rate of the compressed air and the water was controlled by the controlling valves and measured by the flowmeters, respectively.
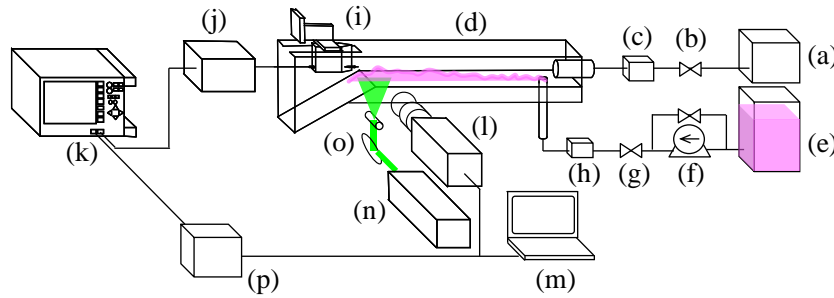
Fig. 7. Experimental setup for thickness measurements. **(a)** Air compressor, **(b)** air control valve, **(c)** air flowmeter, **(d)** acrylic rectangle channel, **(e)** vessel, **(f)** pump, **(g)** water control valve, **(h)** water flowmeter, **(i)** Fs-TOP, **(j)** optical system, **(k)** digital oscilloscope, **(l)** high-speed video camera, **(m)** personal computer (PC), **(n)** YAG-laser, **(o)** laser sheet, and **(p)** function generator.

The Fs-TOP was horizontally installed and vertically traversed. The installed height of the Fs-TOP, H_P, was accurately adjusted by a linear stage (B05-11BM, Suruga Seiki, Shizuoka, Japan). The output signals of the Fs-TOP at every H_P were recorded in a digital oscilloscope (Memory HiCorder 8861-50, Hioki, Nagano, Japan) through the optical system, and then the liquid-film ratios β and wave velocities C_w at H_P were obtained. We used a high-speed video camera (Phantom, 4000 [fps], 576×576 [pixels], 6.7 [μm/pixel]) to verify the film thickness and wave velocity by both the shadow graph

method and the LIF method.

Regarding the thickness measurement, we quantitatively evaluated the relationship between the visualized film thicknesses and the β values. A continuous wave (CW) YAG-laser (Elite, Laser Quantum, Stockport, UK; $\lambda = 532$ [nm]) (Fig. 8n) was sheeted and irradiated from the bottom of the channel, vertically. The camera was focused on the planar sheet. The sheeted laser (1-mm thick) excited a fluorescent dye (Rhodamine B, Fujifilm Wako Pure Chemical Corp., Tokyo; $\lambda_{ex} = 535$ [nm], $\lambda_{em} = 575$ [nm]) that was dissolved in the liquid film, and the fluorescence emission of the liquid surface was extracted through a 545-nm longpass filter. We were thus able to capture tomography images of the wave contours at the slice thickness of 1 [mm]. Note that a meniscus on the channel-side wall was not observed in this experiment, because the width of the liquid film was approx. 5 [mm] and was narrow enough for the channel width. The liquid film flowed at the center of the channel width and the Fs-TOP was also installed at center. The output signals from the Fs-TOP and the high-speed camera were perfectly synchronized by using a function generator (Fig. 7p).

Regarding wave-velocity measurements, we also compared the results of the visualization and those obtained with the Fs-TOP by means of a different setup (Fig. 8). In this test, the CW YAG-laser was used as the light source in the optical system of the Fs-TOP, in order to visualize the time and position at which the Fs-TOP starts to contact the film surface. As mentioned above, some of the light reaching the tip of the fiber is refracted and propagated to the outside phase. Due to the Fs-TOP's wedge-lensed tip, the distribution of propagation intensity values in a region in which the optical intensity is increased approaching the tip is formed [38]. Such an exciting 'spotlight' illuminates just around the tip of the Fs-TOP, so that bright fluorescence is detected only when the tip is positioned on the film surface (Fig. 9). The shadow graph of the liquid film is also obtained simultaneously by using a metal-halide lamp (MME-250, Moritex Corp., Saitama, Japan) as a backlight. The experimental conditions are summarized in Tables 1 and 2. In accord with Fukano's classification of flow patterns, our experiments were

conducted in the region of the two-dimensional flow and pebble-wave flow [15, 39]. As shown in Table 2, we chose higher air velocity tip the wave-velocity measurement in order to disturb the liquid film surface, more significantly.
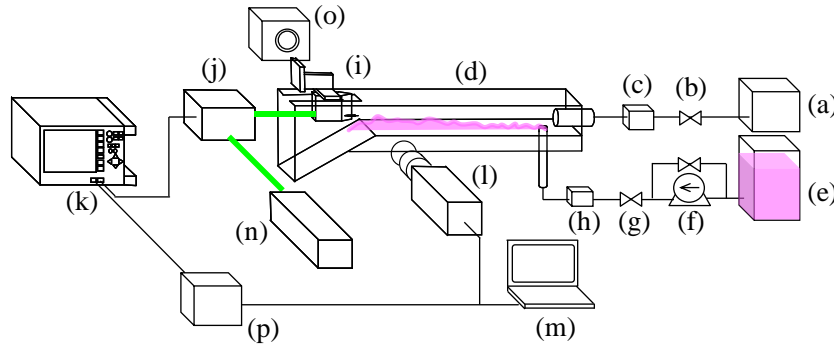
Fig. 8. Experimental setup for wave-velocity measurement. **(a)** Air compressor, **(b)** air control valve, **(c)** air flowmeter, **(d)** acrylic rectangle channel, **(e)** vessel, **(f)** pump, **(g)** water control valve, **(h)** water flowmeter, **(i)** Fs-TOP, **(j)** optical system, **(k)** digital oscilloscope, **(l)** high-speed video camera, **(m)** PC, **(n)** YAG laser, **(o)** metal-halide lamp, and **(p)** function generator.

(i) Not positioning   (ii) Positioning on the surface
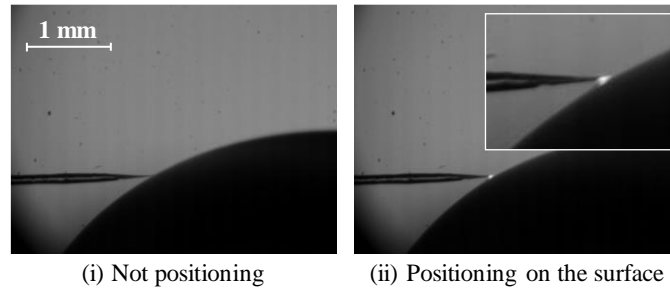
Fig. 9. Graphical detection of the tip position on the film surface.

Table 1. Experimental conditions for the thickness measurements

Air flow rate [L/min]	150
Water flow rate [L/min]	0.12
Gas superficial velocity [m/s]	4.2
Liquid superficial velocity [m/s]	0.003
Installed height of Fs-TOP, H_P [μm]	63, 163, 263, 313, 363, 413, 463, 513, 563, 663, 763, 863, 963, 1063
Sampling rate of Fs-TOP, f_P [kHz]	100
Measurement time of Fs-TOP, T_t [s]	2
Fluorescent dye	Rhodamine-B
Laser wavelength [nm]	532 (CW:YAG)
Fluorescence wavelength [nm]	575
Cutoff wavelength of high-pass filter [nm]	545
Frame rate, f_r [fps]	4000
Frame size [pixel]	576×576

Table 2. Experimental conditions for the wave-velocity measurements

Air flow rate [L/min]	160-210
Water flow rate [L/min]	0.09-0.14
Gas superficial velocity [m/s]	4.5-5.9
Liquid superficial velocity [mm/s]	2.25-3.50
Installed height of Fs-TOP, H_P [μm]	1220-1550
Sampling rate of Fs-TOP, f_P [MHz]	10
Measurement time of Fs-TOP, T_t [s]	2
Fluorescent dye	Rhodamine-B
Laser wavelength [nm]	532 (CW:YAG)
Fluorescence wavelength [nm]	575
Cutoff wavelength of high-pass filter [nm]	545
Frame rate, f_r [fps]	10000
Frame size [pixel]	832×720

4. Results and discussion

4.1. The measurement of liquid-film thickness by the Fs-TOP

Figure 10 is a typical visualization image from the experiment. The fluorescence of the liquid-film surface was clear with the use of the LIF method. The average thickness δ_{mean} was calculated by image processing of the analysis area 'A,' which was prepared right in front of the sensing tip of the Fs-TOP as shown in Figure 10. In the image processing, (1) the brightness of each pixel was searched from top (the air side) to bottom

(the liquid film side) in the vertical direction of the area-A. The bright pixel which indicated the liquid film surface was found by the threshold. (2) The height of the bright pixel was calculated from left to right in the horizontal direction of the area-A. (3) The sum of the heights was averaged by the width of the area-A. (4) The spatial-average thickness was output. If there was no liquid film (air single-phase flow), the fluorescence of the liquid film did not occur and the liquid film was calculated as zero. An example of the time-series thickness in 0.2 s is depicted in Figure 11. Until the measurement, the thickness of the generated liquid film δ fluctuated between 0.2 and 0.8 [mm], and the δ_{mean} was 0.46 [mm] for the total measurement time of 2 s. Based on the principles of the Fs-TOP, the thickness could be obtained simply by determining the H_P at which β=0.5, and this result was 0.50 [mm] by a regression analysis. These data agree well with each other, but this agreement is not generalizable because the measurement was conducted under well-controlled conditions. We discuss the uncertainty and calibration for β to determine the robustness of the thickness measurements by the Fs-TOP later in this paper.
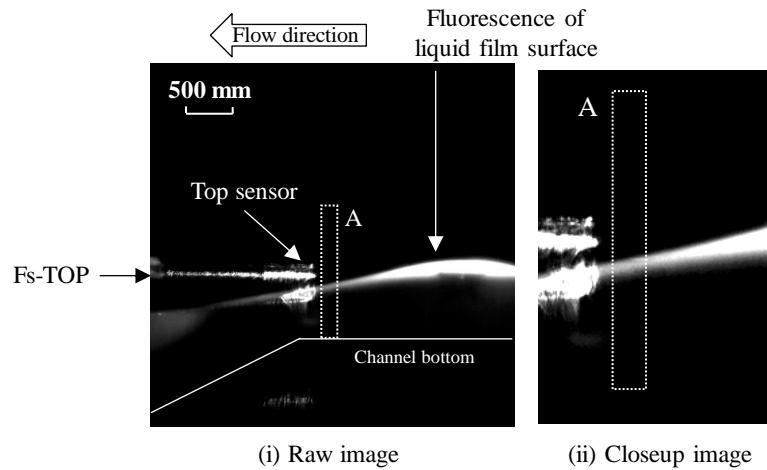
Fig. 10. A typical visualization image from the LIF method.
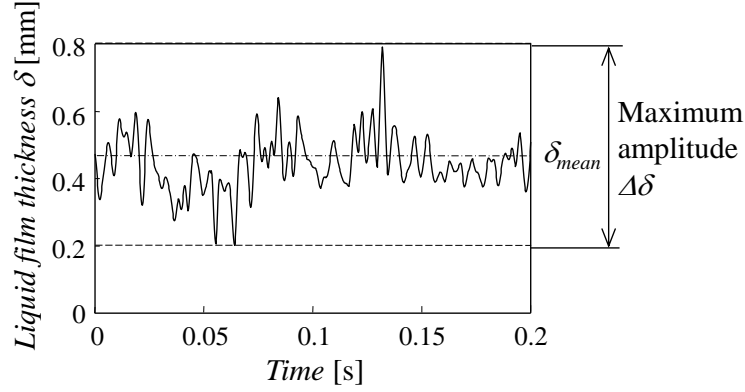
Fig. 11. Analysis results of time-series liquid-film thickness values from the image processing.

Using the visualized results of δ_{mean} and the maximum amplitude, $\Delta\delta$, H_P was normalized by the following equation:

$$R_P = \frac{H_P - \delta_{mean}}{\Delta\delta} \tag{7}$$

where R_P is the relative height [−]. According to the definition, the relative height R_P is equal to 0 when H_P is equal to δ_{mean}. Figure 12-i shows experimental results of the relationship between R_P and β in different R_P ranges. The plots express the experimental results. The dotted line was calculated by using the captured images and is drawn as the visualization line (see Appendix B). The visualization line shows how the plots should be aligned; however, the dots are larger values than the visualization line.

A solid line in Figure 12-ii shows a fitting line of the dots. The fitting line was calculated by the least-square method with a fixed gradient that was calculated from the R_P variation of the visualization line in the β range of 0.4–0.6. This fitting line passes $R_P = 0$ when $\beta = 0.56$. These results mean that the β obtained from the output signal of the Fs-TOP was overestimated. Indeed, problems of this nature appear frequently in optical fiber probing [40] and are the result of the physical interaction between the sensing tip of

the Fs-TOP and the gas-liquid interface; i.e., interface deformation and liquid deposited on the probe tip.

(i) $-0.5 < R_P < 1$

(ii) $-0.05 < R_P < 0.05$
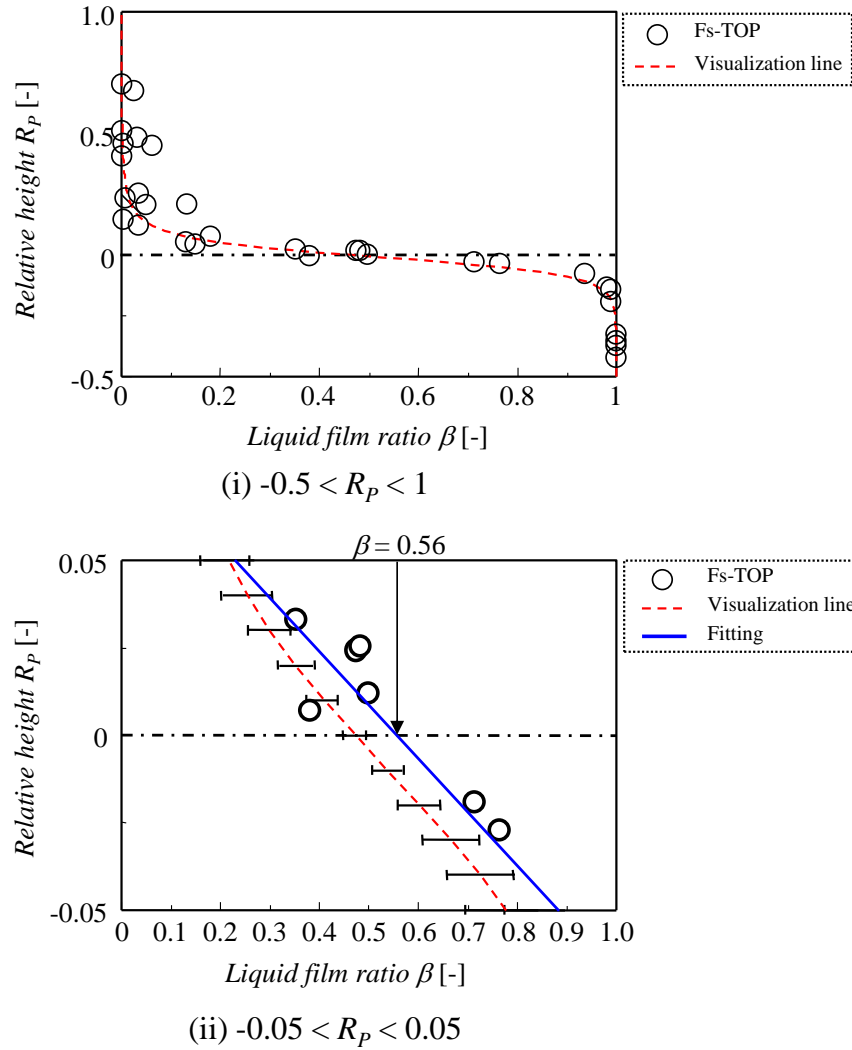
Fig. 12. Experimental results regarding the relationship between the relative height R_P and the liquid-film ratio β.

We assumed that the overestimation of the liquid-film ratio in Figure 12 was caused by overestimating the measurement time T_L in Eq. (1). Focusing on the contact effect between the Fs-TOP and the gas-liquid interface, we defined the entire overestimation by the following equation:

$$T_{delay} = \sum_{p=1}^{k} \left(\frac{l_p}{C_p} + t_{dw} \right) \tag{8}$$

where T_{delay} is the overestimated time for T_L, k is the number of measured waves, p is an integer, l is the dynamic meniscus length, and t_{dw} is the time of de-wetting. The first term on the right-hand side of Eq. (8) indicates the time delay caused by deformation of the gas-liquid interface and the second term indicates the time delay caused by the de-wetting process.

Figure 13 shows simulated signals of the three-dimensional ray tracing (3DRT) with consideration of the deformation of the gas-liquid interface [38]. The meniscus is formed around the sensing tip immediately before the tip penetrates the interface from liquid to gas, and thus the residence time of the tip in the liquid was prolonged [41]. Here, the dynamic meniscus length l is in the order of the radius of the fiber r [42] or is expressed as $\sim r\mathrm{Ca}^{\frac{1}{3}}$ [43], which suggests the deformation depth before penetration; therefore, the delay time before penetration can be estimated as l/C (where C is the wave velocity). This time period is several microseconds at most with the use of the Fs-TOP.

Another factor in the overestimation is the de-wetting process during the tip penetration, as shown in Figure 14. A thin liquid film is formed around the Fs-TOP tip due to liquid entrainment, the thickness of which is expressed as $\sim r\mathrm{Ca}^{\frac{2}{3}}$ [43]. The liquid film remains along the latency length [44–46] of the Fs-TOP, and this the residence time is further lengthened (see the Supplementary Movie). The time of de-wetting, i.e., t_{dw} [s] is difficult to evaluate because it is derived from the wettability around the tip (which varies among probes), but we have empirically estimated this by calculating the decay time of the fluorescence at the tip in Figure 14 based on the assumption that the quenching indicates nothing but the de-wetting process. The average of this random error results in a <150-μs of the decay time t_{dw}.

Over 800 waves have been detected in the thickness measurement, and those delays

accumulate with every detection of the rear surface of the waves. According to Eq. (8), the first term is a minor contribution to the overestimation of β by <0.5% (13 μs), and the second term is approx. 6% (150 μs). Consequently, δ_{mean} could be calculated with H_P at β=0.56.
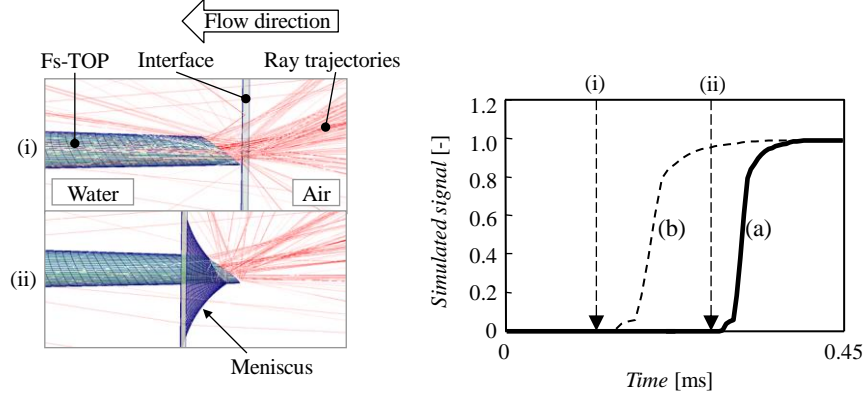
Fig. 13. Simulated signals of the 3DRT with considering a deformation of the gas-liquid interface: (a) a signal demonstrating the residence time prolonged by the meniscus, (b) a signal without the meniscus.
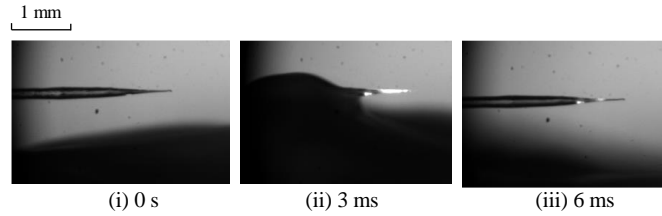
Fig. 14. Visualized de-wetting process by the LIF method. Fluorescence is emitted from liquids remaining around the Fs-TOP tip, and it decays with de-wetting. These photos were obtained in the wave-velocity measurement experiment.

We have analytically calculated the relationship between R_P and β. Artificial wave heights δ_r [−] were generated based on the superposition of linear progressive waves by the following equation:

$$\delta_r(t) = \sum_{i=1}^{100} \left[\sqrt{S(\overline{\omega_i})\Delta\omega_i} \cos\left(\overline{\omega_i}t - \phi_i\right) \right] \tag{9}$$

$$S(\omega) = 2AB \left[\frac{1}{B^2 + (\omega + \omega_0)^2} + \frac{1}{B^2 + (\omega - \omega_0)^2} \right] \qquad (10)$$

Here, i is the waveform number [−], S is a spectrum [−], ω is an angular frequency [rad/s], and ϕ_i is a phase [−]. The spectrum S is calculated by Eq. (10), where A and B are constant numbers. Random numbers from 0 to 1 are substituted for ω_i and ϕ_i, respectively. $\overline{\omega_i}$ is defined as $\overline{\omega_i} = (\omega_{i-1} + \omega_i)/2$ and $\Delta\omega$ is defined as $\Delta\omega = \omega_i - \omega_{i-1}$. According to Eq. (10) with $A=1$ and $B=0.5$, 100 random waves are generated. A hypothetical Fs-TOP measures the random wave in Figure 15 at each installed height H_P at 0 to 1 (cf. Appendix B). The corrected liquid-film ratio β' including the above overestimation time T_{delay} in Eq. (8) is calculated at every H_P value by the following modified equation:

$$\beta' = \frac{\sum T_L + T_{delay}}{T_t} \qquad (11)$$

We measured 1,000 random waves and averaged them (Fig. 15). Figure 16-i is a typical result analyzed from one waveform of the random waves, and it illustrates a relationship between the relative height R_P and the liquid-film ratio β'. For the evaluation of β', the overestimated time T_{delay} is calculated from Eq. (8) with the de-wetting time $t_{dw}=150$ [μs] and $l_p / C_p \approx 0$. From the result, the relative height R_P is almost equal to 0 when $\beta'=0.56$. Moreover, the maximum amplitude of the liquid-film thickness $\Delta\delta$ can be estimated by the difference of H_P in the β' range between 0 and 1.

Figure 16-ii provides the analysis results from the total number of the random waves, and it shows a probability density function (PDF) of the relative height R_P when $\beta'=0.56$. The PDF of the relative height R_P is highest at $R_P =0$. Therefore, the overestimated time T_{delay} is used to introduce the overestimation effect of β'. Calculating

R_P when β'=0.56 from the measurements, we can estimate the relative thickness of the liquid-film flow. A solid line in the figure is a fitting result of Gaussian distribution with $\mu = 0$ and $\sigma = 0.01$. Thus, the accuracy of the measurement results in $R_P = 0 \pm 0.03$ (3σ) when β'=0.56. $(H_P-\delta_{\text{mean}})$ in Eq. (7) indicates measurement error of the average thickness when $R_P = 0 \pm 0.03$; therefore, the measurement error in the average thickness is calculated from 3% of the maximum amplitude $\Delta\delta$.
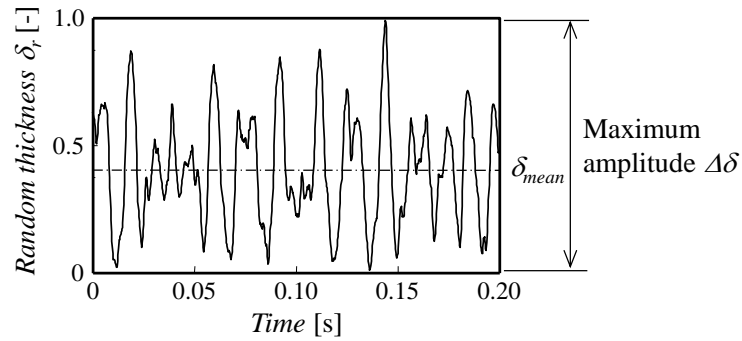
Fig. 15. A demonstration of the random thickness.
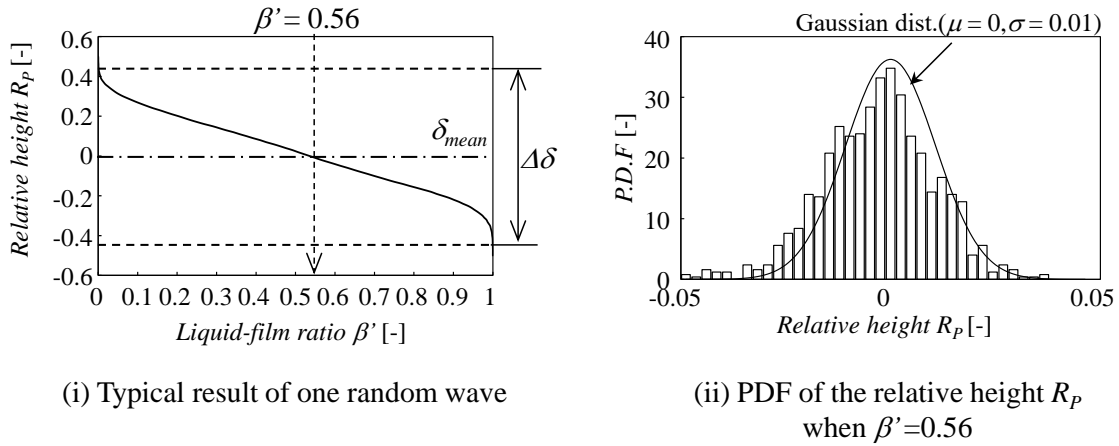
(i) Typical result of one random wave

(ii) PDF of the relative height R_P when β'=0.56

Fig. 16. Analysis results of random waves including the overestimation effect.

4.2. The measurement of wave velocities by the Fs-TOP

Figure 17-i shows a raw signal acquired by the Fs-TOP. The two sensors detected a two-step decrease in the output signal (see also simulated signal in Appendix C). Figure

17-ii is a histogram of the output signal; the gas level V_G and the liquid level V_L can be determined from the first and second maximum peaks of the histogram. A groove level, V_{groove} was also determined from the third peak at which the groove sensor (S2) was covered by the gas-liquid interface (Fig. 3).

For the calculation of the wave velocity using Eq. (6), the time lag Δt was defined by the interval in which the output voltage decreased from V_{th2} to V_{th3}. The higher threshold V_{th2} was calculated by Eq. (5), and the middle threshold V_{th3} was calculated by the following equation:

$$V_{th3} = V_{groove} + \gamma(V_G - V_L) \tag{12}$$

where the determination rate γ was 10% used to find midpoints of the steep decline in the signal, as shown in Figure 17-i.

For the confirmation of the Fs-TOP's measurement accuracy, visualized results of the wave velocity were output from the image analysis. Figure 18 presents visualized images by the back-light method. Those images were captured by the high-speed video camera in 1.625 [ms] and were binarized. The gas-liquid interface of the liquid film is clearly visualized. We calculated the displacement of the interfacial wave Δx [m] by finding the maximum cross-correlation of a wave shape. The visualized result of the wave velocity C_w [m/s] was calculated from the following equation:

$$C_w = \Delta x f_r \tag{13}$$

Here, f_r [Hz] is the frame rate of the high-speed video camera. The wave velocities were calculated from the visualized images right before the Fs-TOP contacted the liquid film, and they were averaged.

Figure 19 illustrates the results of our comparison of the measured local interfacial velocity C_i and the visualized wave velocity C_w. The variations become large as the flow rates increase, because both interfacial motion and wave velocity strongly correlate with the flow rates [15]. The C_w is a spatial average of the entire disturbance wave, which has a physically different velocity from C_i; we thus assume that the local interfacial velocity can be representative of the wave velocity as long as the waves are in the same direction. In fact, the local interfacial velocity values obtained with the Fs-TOP were in good agreement with the visualized wave velocities, within 15% accuracy. We considered that the contact effect of the Fs-TOP on the results was included but it was small. We discuss the uncertainty of the wave velocity measurements in more detail.

(i) Output signal   (ii) Histogram
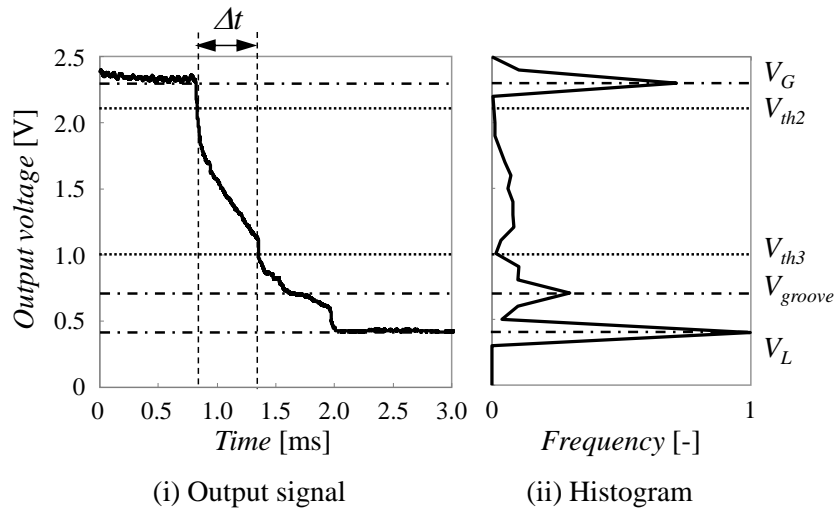
Fig. 18. An output signal from the Fs-TOP and the histogram.
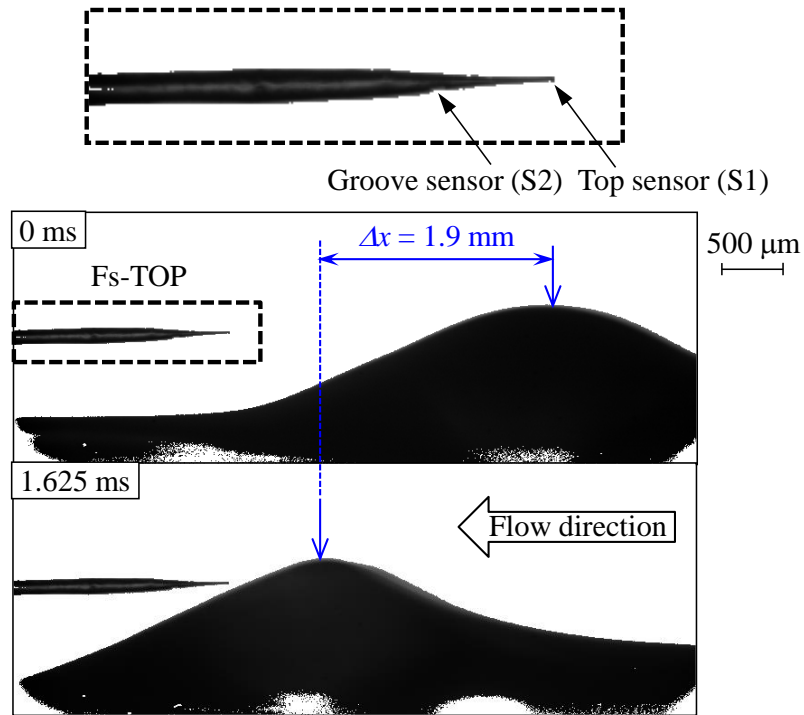
Fig. 18. Visualized images obtained by the shadowgraph method.
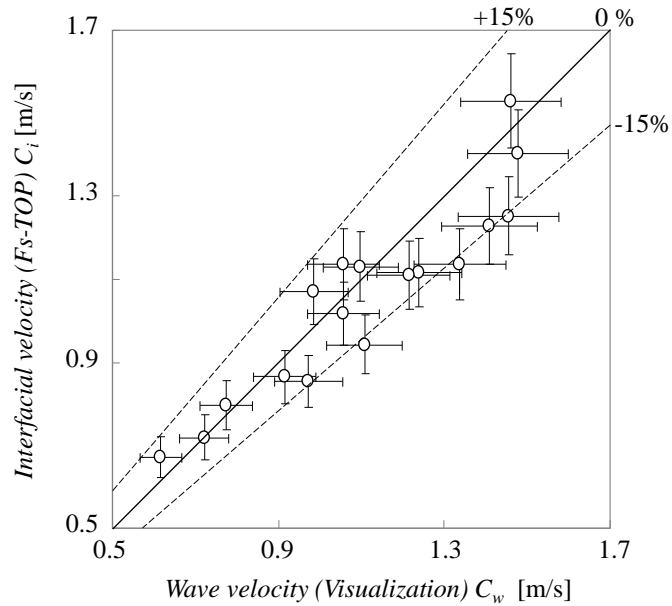
Fig. 19. Comparison of the measured results and the visualized results. Error bars: Std. deviations of the respective results.

Here, the uncertainty of the visualization was caused by a pixel error of the high-speed camera with the spatial resolution of 7.04 [μm]. The frame rate was 10,000 [fps]

which indicated the temporal resolution, and thus those limitations of both the spatial resolution and the temporal resolution caused the uncertainty of C_w. The C_w uncertainty value was much smaller than the measured velocities (1% at most). The error from the visualization is thus negligible.

A faulty threshold decision in the signal processing is a major uncertainty which arises due to the liquid deposited on the Fs-TOP sensors; its mechanism was already shown in the uncertainty analysis regarding thickness measurement, and the liquid usually dries out immediately after being exposed in the gas phase. Although the Fs-TOP detects so many waves in a row, a very small amount of the liquid can remain on the sensors. A simulation example is presented in Figure 20. Ellipsoidal cap-shaped droplets exist on the sensor (S1) of the Fs-TOP, and the cap height has been used as a parameter to survey whether the gas-phase level increases or decreases with the droplets' shape. There are many irregular reflections in the cap, and the output signal inevitably increases unless the sensor is dry. V_G, V_{th2}, V_{groove}, and V_{th3} can be faulty values in such conditions, and this reduces the accuracy of Δt (Fig. 21). Although this uncertainty is unpredictable and difficult to remove from statistical analyses, our results indicate that this effect does not make the measurement difference exceed ±15%. We recommend pretreatment of the optical fiber with a water repellent to minimize this value, because only the wettability causes the major uncertainty, regardless of the flow condition. Further investigations are required, but our new method can be one of the effective ways to elucidate unknowable liquid-film flows.

The deceleration effect [41] — which is often controversial — during the piercing of the front of the wave is minor because the velocity measurement is finished rapidly in this method. In our experiment, the wave propagation was fast enough compared with the interfacial deformation speed due to the surface tension. The deceleration effect can therefore be observed in a viscosity-dominant condition such as a viscous wave flow.

Either the flow around the Fs-TOP or the fixing position of the Fs-TOP makes the sensing tip oscillate slightly, and thus a quantification of the uncertainties due to the

displacing of the fiber-tip is necessary. We confirmed that the amplitude of the vertical oscillation was ±4.2 [μm], which we evaluated by visualization with a spatial resolution of 1.9 [μm]; we then simulated an effect of the oscillation on the output signal. A first bending mode of an optical fiber is modeled by the deflection curve and implemented by the 3DRT simulation. Figure 22 illustrates the relationship between a vertical displacement D of the fiber tip and the output signal. Regarding V_G for example, the dotted line in Figure 23 was obtained when the vertical displacement was equal to 0 (no oscillation).

On the other hand, the output signal decreased with the displacement, because some of the light path in the optical fiber was cut off by the bending. The decrease in the output signal was <5% within the range of the visualized displacement in our experiments. It is applicable to not only V_G but also all output levels. Nevertheless, this effect is essentially minor if the vibration velocity is not significantly larger than the interfacial velocity. The effect can also be avoided by reinforcing the installation of the Fs-TOP.
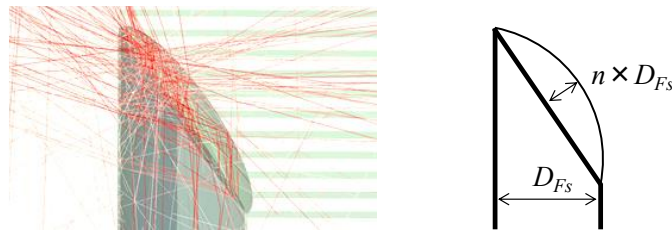
(i) Simulated model for uncertainty of threshold decision.
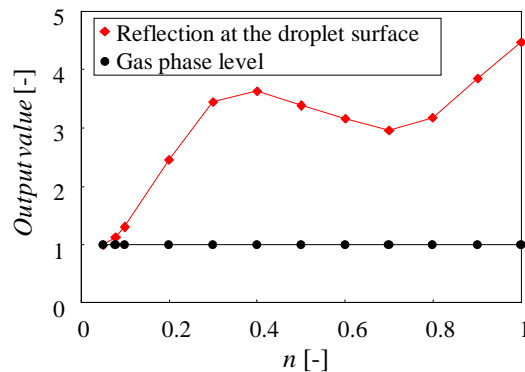
(ii) Simulated uncertainty for V_G decision.

Fig. 20. Uncertainty analysis of the signal processing threshold decision.

	S1 [dry]	S1 [wet]
S2 [dry]		
S2 [wet]		
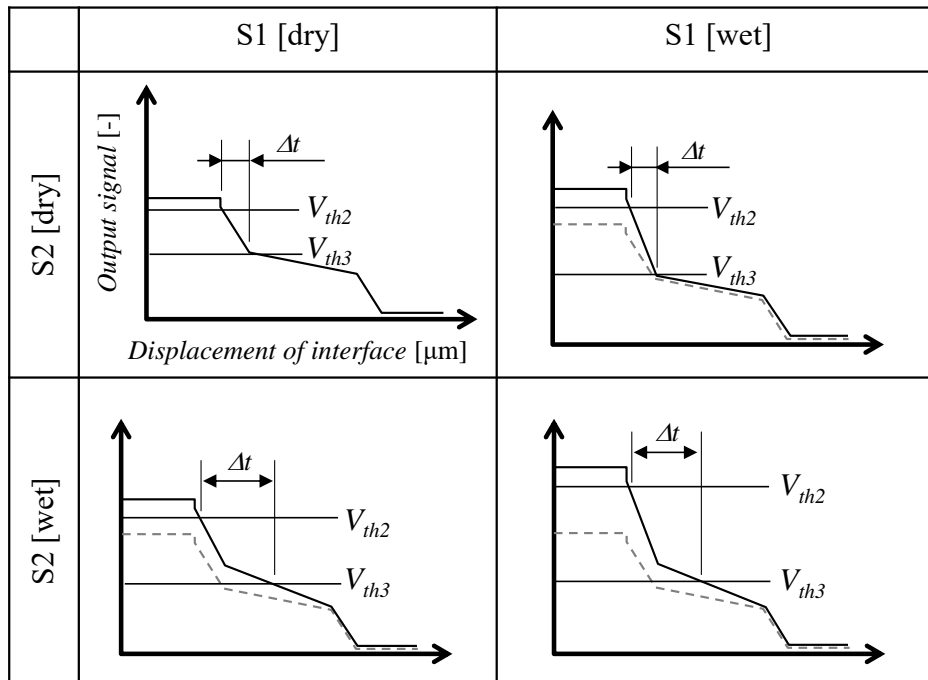
Fig. 21. Uncertainty of Δt derived by liquid deposition. Faulty V_{th2} and V_{th3} decisions are considered qualitatively, based on Figure 20 and Appendix C. The matrix shows the combination of the sensors' conditions.

Cylindrical optical-fiber-probe
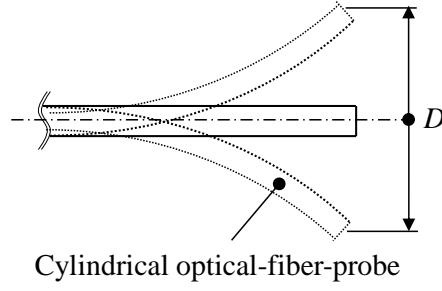
(i) Simulated model for evaluation of a bending influence of optical fiber in the air-single phase.

Vertical displacement of sensing tip D [μm]
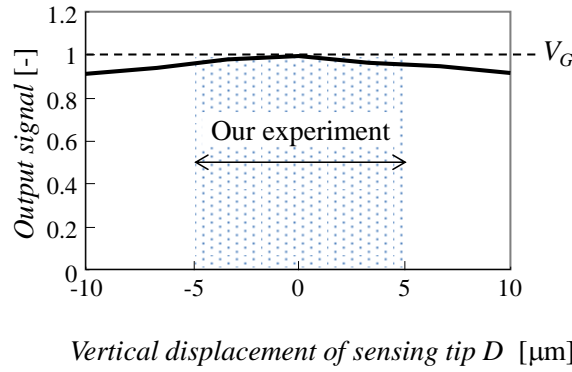
(ii) Simulated uncertainty for output signals in the air single-phase.

Fig. 22. Influence of the bending of the optical fiber on the output signal.

5. Conclusions

We have proposed a new method for measuring liquid-film flows by the Fs-TOP with high spatial resolution. The Fs-TOP is fixed horizontally to the channel bottom and is traversed vertically to investigate the wave height at the installed position. The liquid-film ratio β was calculated from the output signals of the Fs-TOP in a verification test for the measurement of film thicknesses. We have estimated the thickness as the relative height R_P of the Fs-TOP, but this has a tendency to result in an overestimation against the visualization result (the time delay of the rear interface detection) because of the meniscus formation on the sensing tip. According to the uncertainty analysis, the de-wetting time is the dominant factor. The time per wave detection evaluated by the LIF method is <150 [μs], which is the quenching time of the fluorescence around the sensing tip. Considering this effect, the mean value of the wave height can be measured at $\beta = 0.56$ and the

measurement error in the average thickness δ_{mean} is calculated by 3% of the maximum amplitude $\varDelta\delta$.

The relationship between the R_P and β values was also analytically calculated, enabling the estimation of the maximum amplitude and the arbitrary wave height as well. In our verification test for the wave velocity measurement, the results measured by the Fs-TOP were in good agreement with the visualized results within 15% accuracy, which may have been due to the liquid deposition on the sensors during frequent wave detection. It is difficult to remove this uncertainty statistically, but a simple and effective solution is water repellent pretreatment of the optical fiber. There is no similar method to reveal the local interfacial velocity, and our new method is preferable in particular for monitoring instantaneous wave phenomena. In light of these abilities, our new method shows significant effectiveness for measuring unknowable liquid-film flows.

Nomenclature

A	[−]	constant
B	[−]	constant
β	[−]	liquid-film ratio
β'	[−]	liquid-film ratio
C	[m/s]	wave velocity
C_i	[m/s]	local interfacial velocity
C_w	[m/s]	wave velocity
Ca	[−]	capillary number
$\varDelta\delta$	[m]	maximum amplitude
$\varDelta t$	[s]	time lag of a phase detection
$\varDelta x$	[m]	displacement of the interfacial wave
δ_{mean}	[m]	average thickness
δ_r	[m]	artificial wave height
f_i	[−]	frequency
f_r	[Hz]	frame rate

f_s	[Hz] sampling rate
ϕ_i	[rad] phase
γ	[−] determination rate
H_P	[m] installed height of Fs-TOP
i	[−] waveform number
k	[−] number of measured waves
L_P	[m] sensor gap between a sensing-tip and a groove of Fs-TOP
l	[m] length
λ	[m] wavelength
λ_{em}	[m] emission wavelength
λ_{ex}	[m] excitation wavelength
n	[−] detection number
n_t	[−] number of discrete data
p	[−] integer
R_P	[−] relative height of Fs-TOP
r	[m] radius
S	[−] spectrum
T_{delay}	[s] overestimated time
T_L	[s] measurement time
T_t	[s] total measurement time
t_{dw}	[s] time of de-wetting
V	[V] output voltage
V_{groove}	[V] groove level
V_{th1}	[V] lower threshold
V_{th2}	[V] higher threshold
V_{th3}	[V] middle threshold
ω	[rad/s] angular frequency

REFERENCES

[1] Hewitt, G.F., Govan, A.H., Phenomenological modelling of non-equilibrium flows with phase change, Int. J. Heat Mass Transfer, 33(2) (1990) 229-242.

[2] Tanasawa, I., Advances in condensation heat transfer, Advances in Heat Transfer, 21 (1991) 55-139.

[3] Brunazzi, E., Paglianti, A., Liquid-film mass-transfer coefficient in a column equipped with structured packings, Ind. Eng. Chem. Res., 36 (1997) 3792-3799.

[4] Hall-Taylor, N.S., Nedderman, R.M., The coalescence of disturbance waves in annular two phase flow, Chem. Eng. Sci., 23(6) (1968) 551-564.

[5] Hazuku, T., Takamasa, T., Matsumoto, Y., Experimental study on axial development of liquid film in vertical upward annular two-phase flow, Int. J. Multiphase Flow, 34 (2008) 111-127.

[6] Fukano, T., Mori, S., Nakagawa, T., Fluctuation characteristics of heating surface temperature near an obstacle in transient boiling two-phase flow in a vertical annular channel, Nucl. Eng. and Des., 219 (2003) 47-60.

[7] Fukano, T., Mori, S., Akamatsu, S., Baba, A., Relation between temperature fluctuation of a heating surface and generation of drypatch caused by a cylindrical spacer in a vertical boiling two-phase upward flow in a narrow annular channel, Nuclear Eng. Des., 217(1-2) (2002) 81-90.

[8] Akiba, M., Takamasa, T., Morooka, S., Prediction method of critical power by film flow rate measurement and subchannel analysis, Heat Transfer, 34(5) (2005) 309-323.

[9] Nishida, K., Kanazawa, T., Yokomizo, O., Masuhara, Y., spacer effect on liquid film flow and critical power in BWR fuel bundles, J. Nucl. Sci. Technol., 31(3) (1994) 213-221.

[10] Hewitt, G.F., Measurement of two phase flow parameters, Academic Press (1978) 177-179, London.

[11] Koskie, J.E., Mudawar, I. Tiederman, W.G., Parallel-wire probes for measurement of thick liquid films, Int. J. Multiphase Flow, 15 (4) (1989) 521-530.

[12] Ueda, T., Tanaka, H., Measurements of velocity, temperature and velocity fluctuation distributions in falling liquid films, Int. J. Multiphase Flow, 2 (1975) 261-272.

[13] Kamei, T., Serizawa, A., Measurement of 2-dimensional local instantaneous liquid film thickness around simulated nuclear fuel rod by ultrasonic transmission technique, Nucl. Eng. Des., 184 (2-3) (1998) 349–362.

[14] Damsohn, M., Prasser, H.M., High-speed liquid film sensor for two-phase flows with high spatial resolution based on electrical conductance, Flow Measurement and Instrumentation, 20 (2009) 1-14.

[15] Fukano, T., Measurement of time varying thickness of liquid film flowing with high speed gas flow by a constant electric current method (CECM), Nucl. Eng. Des., 184 (2–3), (1998) 363-377.

[16] Skjæraasena, O., Kesana, N. R., X-ray measurements of thin liquid films in gas–liquid pipe flow, International Journal of Multiphase Flow, 131 (2020) 103391.

[17] Hewitt, G.F., Martin, C.J., Wilkes, N.S., Experimental and modeling studies of annular flow in the region between flow reversal and the pressure drop minimum, Physico-Chemical Hydrodynamics, 6–1/2 (1985) 69–86.

[18] Takamasa, T., Kobayashi, K., Measuring interfacial waves on film flowing down tube inner wall using laser focus displacement meter, Int. J. Multiphase Flow, 26 (2000) 1493-1507.

[19] Hazuku, T., Fukamachi, N., Takamasa, T., Hibiki, T., Ishii, M., Measurement of liquid film in microchannels using a laser focus displacement meter, Experiments in Fluids, 38 (2005) 780–788.

[20] Pham, Son H., Kawara, Z., Yokomine, T., Kunugi, T., Measurements of liquid film and droplets of annular two-phase flow on a rod-bundle geometry with spacer, International Journal of Multiphase Flow, 70 (2015) 35-57.

[21] Ohba, K., Origuchi, T., Shimanaka, Y., Multi-fiber optic liquid film sensor. I, Proc. 4th Sensor Symp., (1984) 33-37.

[22] Ohba, K., Origuchi, T., Takada, H., Multi-fiber optic liquid film sensor. II, Proc. 4th Sensor Symp., (1985) 63-67.

[23] Hewitt, G.F., Hall-Taylor, N.S., Annular two-phase flow (first ed.), Pergamon Press, Oxford, New York (1970).

[24] Alekseenko, S., Antipin, V., Cherdantsev, A., Kharlamov, S., Markovich, D., Two-wave structure of liquid film and wave interrelation in annular gas-liquid flow with and without entrainment, Physics of Fluids, 21 (2009) 061701.

[25] Zhao, Y., Markides, C.N., Matar, O.K., Hewitt, G.F., Disturbance wave development in two-phase gas–liquid upwards vertical annular flow, Int. J. Multiphase. Flow, 55 (2013) 111-129.

[26] Zadrazil, I., Markides, C.N., An experimental characterization of liquid films in downwards co-current gas-liquid annular flow by particle image and tracking velocimetry, Int. J. Multiphase Flow, 67 (2014) 42-53.

[27] Vasques, J., Cherdantsev, A., Cherdantsev, M., Isaenkov, S., Hann, D., Comparison of disturbance wave parameters with flow orientation in vertical annular gas-liquid flows in a small pipe, Exp. Therm. Fluid Sci., 97 (2018) 484-501.

[28] Saito, T., Matsuda, K., Ozawa, Y., Oishi, S., Aoshima, S., Measurement of tiny-droplets using a newly developed optical fibre probe microfabricated by femtosecond pulse laser, Meas. Sci. Technol., 20 (2009) 114002.

[29] Mitsuhashi, Y., Saito, T., Measurement of a liquid film inside a steam-water two-fluid nozzle using an optical fiber probe, Transactions of the Japan Society of Refrigerating and Air Conditioning Engineers, 27(2) (2010) 149-160, *in Japanese*.

[30] Hanyu, K., Saito, T., Dynamical mass-transfer process of a CO_2 bubble measured by using LIF/HPTS visualisation and photoelectric probing, Can. J. Chem. Eng., 88 (2010) 551-560.

[31] Sakamoto, A., Saito, T., Robust algorithms for quantifying noisy signals of optical fiber probes employed in industrial-scale practical bubbly flows, Int. J. Multiphase Flow, 41 (2012) 77-90.

[32] Yamada, M., Saito, T., A newly developed photoelectric optical fiber probe for simultaneous measurements of a CO_2 bubble chord length, velocity, and void fraction and the local CO_2 concentration in the surrounding liquid, Flow Measurement and Instrumentation, 27 (2012) 8-19.

[33] Mizushima, Y., Saito, T., Detection method of a position pierced by a single-tip optical fibre probe in bubble measurement, Meas. Sci. Technol., 23(8) (2012) 085308.

[34] Mizushima, Y., Sakamoto, A., Saito, T., Measurement technique of bubble velocity and diameter in a bubble column via Single-Tip Optical-fiber Probing with judgment of the pierced position and angle, Chem. Eng. Sci., 100, (2013) 98-104.

[35] Mizushima, Y., Saito, T., Improving the accuracy of droplet measurement by

optical fiber probe using 3D ray-tracing simulation, J. Chem. Eng. Japan, 52 (2019) 171-178.

[36] Hurlburt, E.T., Newell, T. A., Optical measurement of liquid film thickness and wave velocity in liquid film flows, Exp. in Fluids, 21 (1996) 357-362.

[37] Oliveira, F.S., Yanagihara, J.Y., Pacífico, A.L., Film thickness and wave velocity measurement using reflected laser intensity, J. Braz. Soc. Mech. Sci. & Eng., 28(1) (2006) 30-36.

[38] Sakamoto, A., Saito, T., Computational analysis of responses of a wedge-shaped-tip optical fiber probe in bubble measurement, Rev. Sci. Instrum., 83 (7) (2012) 075107.

[39] Hanratty, T.J., Engen, J.M., Interaction between a turbulent air stream and a moving water surface, AIChE J., 3 (3) (1957) 299-304.

[40] Cartellier, A., Achard, J.L., Local phase detection probes in fluid/fluid two-phase flows, Rev. Sci. Instrum., 62 (1991) 279-303.

[41] Vejražka, J., Večeř, M., Orvalho, S., Sechet, P., Ruzicka, M.C., Cartellier, A., Measurement accuracy of a mono-fibre optical probe in a bubbly flow, Int. J. Multiphase Flow, 36 (2010) 533–548.

[42] Clanet, C., Quéré, D., Onset of menisci, J. Fluid Mech., 460 (2002) 131-149.

[43] Quéré, D., Fluid coating on a fiber, Annu. Rev. Fluid Mech., 31 (1999) 347-384.

[44] Cartellier, A., Barrau, E., Monofibre optical probes for gas detection and gas velocity measurements: Conical probes, Int. J. Multiphase Flow, 24 (1998) 1265-1294.

[45] Cartellier, A., Barrau, E., Monofibre optical probes for gas detection and gas velocity measurements: Optimised sensitive tip, Int. J. Multiphase Flow, 24 (1998) 1295-1315.

[46] Mena, P.C., Rocha, F.A., Teixeira, J.A., Sechet, P., Cartellier, A., Measurement of gas phase characteristics using a monofibre optical probe in a three-phase flow, Chem. Eng. Sci., 63 (2008) 4100-4115.

Appendix A: The design concept of the Fs-TOP

The design concept of the Fs-TOP depends on the measurement object. In this study, we aimed at a measurement of general annular flow via the Fs-TOP. Hence, the assumed velocity and available sampling rate were the basis of our design, as bellow.

The groove position L_P (440 μm) was designed from a distance that was more than the least time difference to calculate targeting velocity. The wave velocity in the annular flow is approximately 1-10 m/s and the sampling rate was 10 MHz. Therefore, at least, L_P was more than 1 μm (= 10 m/s / 10 MHz) (Figure A). Furthermore, in our LIF experiment in Chapter 3, the distance between the tip (S1) and the groove (S2) was required to be long enough to distinguish. We thus decided L_P = 440 μm due to such an experimental circumstance.

The groove width (50 μm) was designed from the length to sample at least 10 points in the above condition. The number of data points detected by the groove width was thus estimated 50 points (= 10 MHz / (10 m/s / 50 μm)). We determined the groove depth to ensure both the mechanical strength and the signal-to-noise ratio based on the past study [28].

(i) Minimum required length for L_P (ii) Too short L_P
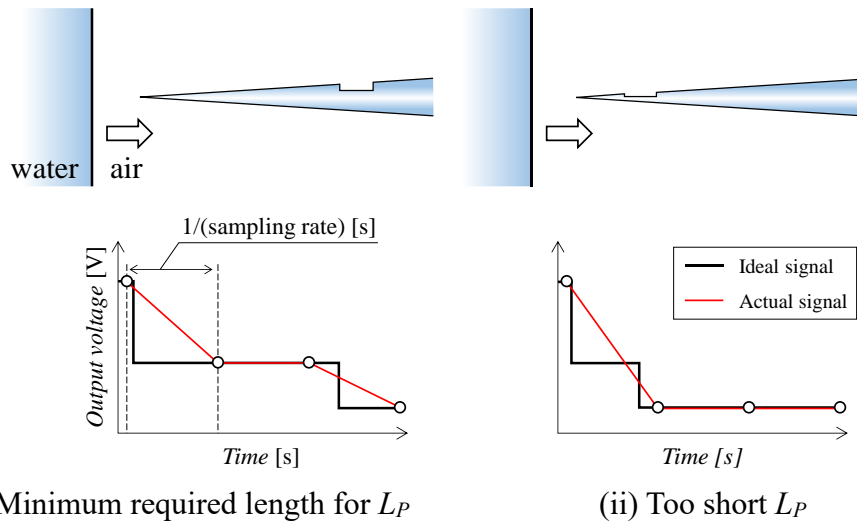
Fig. A. A schematic of L_P decision. If L_P is enough (i), the output is a two-step signal that enables an estimate of the velocity. If L_P is too short (ii), the velocity measurement becomes impossible by the proposed signal processing.

Appendix B: The calculation process of the visualization line

Figure B1 presents the calculation process of the visualization line from the visualization result of the liquid-film thickness (Fig. 13). For the visualized results of the time-series thickness, a hypothetical Fs-TOP was set with the installed height $H_P{'}$. Thus, using the $H_P{'}$ as the threshold, a hypothetical signal was simply calculated, and the liquid-film rate β was output. The hypothetical installed height $H_P{'}$ was traversed from the minimum thickness to the maximum thickness, with the range of the relative height R_P of 0~1. Figure B2 provides a flowchart of the processing. Finally, the visualization line of Figure 13 was output from the average of the liquid-film rate in the total number of visualization data, and the error bar was calculated from the standard deviation of the total number of visualization data.
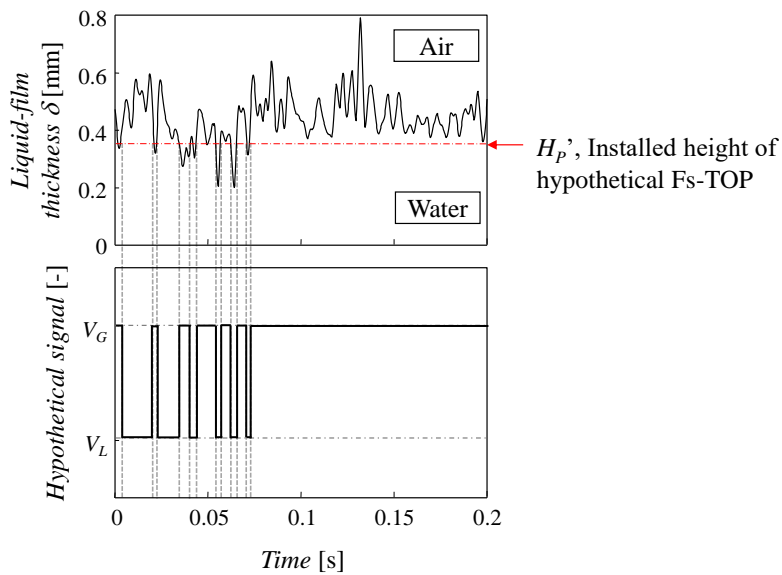
Fig. B1. Calculation process of the visualization line.
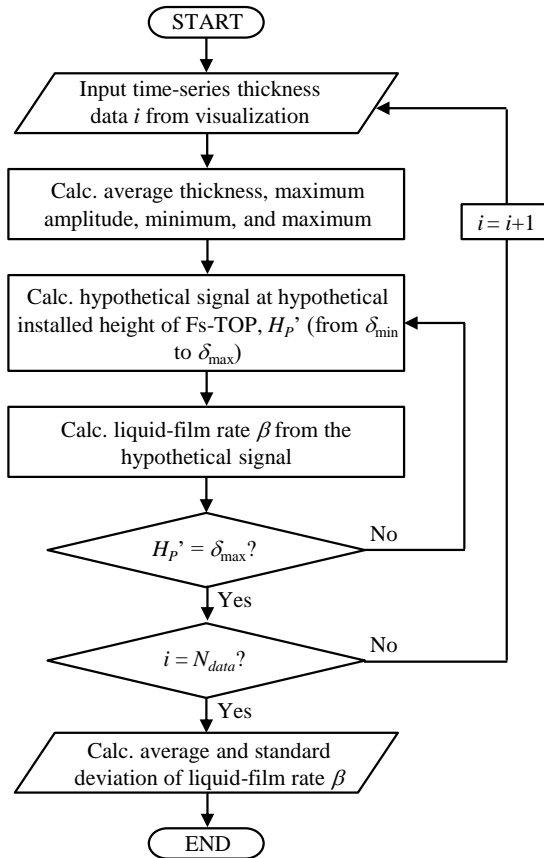
Fig. B2. A flowchart of the processing for the visualization line.

Appendix C: The 3D ray-tracing (3DRT) simulation

Figure C1 illustrates a demonstration of a 3D model of the Fs-TOP by our 3DRT. The simulator can simultaneously calculate ray trajectories and ray energy values in geometrical models of the optical fiber and the phases, and thus the returned beams in the measurement are quantitatively evaluated from the optical interaction between the top sensor, the groove sensor, and the gas-liquid interface. The color contour in Figure B1a is the ray-energy distribution discharged from the Fs-TOP to the water. Notably, the ray-energy density surrounding the sensors is high.

Figure C2 shows a simulated signal from the Fs-TOP, simulating the time point at which the flat gas-liquid interface passes the top sensor and the groove sensor. The horizontal axis is the displacement of the gas-liquid interface. According to this figure, the simulated signal behaves as a two-step decrease from the gas level V_G to the liquid level V_L. This is because the simulated signal includes the returned beams detected from both sensors. When the top sensor is positioned from the air to the water at the displacement of L_1, the simulated signal decreases from the gas level V'_G to the middle level V'_{groove}. After that, the groove sensor is immediately covered by the water at the displacement of L_2. The simulated signal then decreases to the liquid level V'_L. In the actual signal of the time-series voltage, the difference in the two-step decrease ($L_2 - L_1$) is exactly equal to the time lag Δt in which the gas-liquid interface passes through the sensor gap L_P. The interfacial velocity is thus calculated by analyzing the time lag from the output signal.
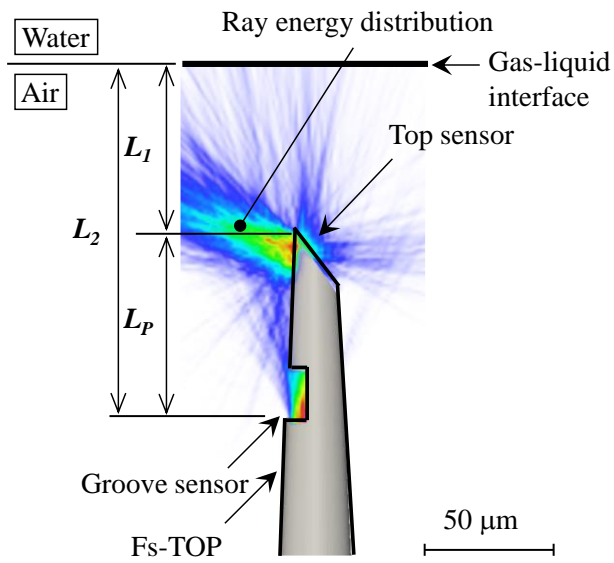
Fig. C1. A 3D model of the Fs-TOP by 3DRT.
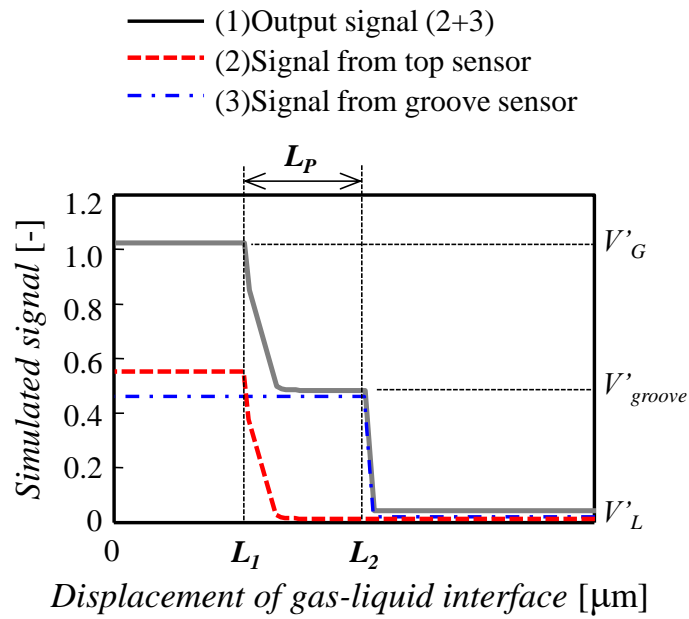
Fig. C2. A simulated signal of the Fs-TOP by 3DRT.